Ablation phenomena by intense terahertz vortex beam

You Wei Wang[1,2] · Sadashi Segawa[1] · Tomoki Shimizu[1] · Verdad C. Agulto[1] · Valynn Katrine Mag-usara[1] · Kosaku Kato[1] · Katsuhiko Miyamoto[3] · Takashige Omatsu[3] · Kotaro Makino[4] · Junji Tominaga[4] · Goro Isoyama[5] · Makoto Asakawa[2] · Makoto Nakajima[1]

Abstract

We have successfully generated a highly efficient terahertz (THz) vortex beam by using a THz free-electron laser incident to a spiral phase plate (SPP). The singularity at the center is apparently observed in the image of the transmitted beam after the SPP. We demonstrate the THz vortex beam-induced laser ablation on phase change materials, $Ge_2Sb_2Te_5$ and $GeTe/Sb_2Te_3$. The ablation marks show an annular spatial form and modulated laser-induced periodic surface structures (LIPSS) pattern. These observations can be attributed to the torque of the THz vortex.

Keywords Vortex beam · Terahertz wave · Ablation · Free electron laser · LIPSS

1 Introduction

Recent advances in terahertz (THz) science and engineering, including THz spectroscopy, imaging, and the applications of THz waves in general, have attracted much attention [1-19]. Development of high-intensity terahertz pulse excitation can induce nonlinear optical effects including ablation phenomena. Recently, our group reported THz pulse-induced ablation and laser-induced periodic surface structures (LIPSS) formed using THz free electron laser [20].

An optical vortex is light with a spiral wavefront, whereas the wavefront of normal light is flat or spherical. The existence of this optical vortex was revealed 30 years ago [21]. Optical vortex has been used in optical tweezers, optical communication, data storage, material processing, metrology, and astronomy [22-26]. There are many methods to generate an optical vortex such as via hybrid phase plates, metasurface holograms and geometric phase metasurfaces [27-29]. Among those methods is directing a Gaussian beam to a spiral phase plate (SPP), which is a phase plate whose thickness changes in the azimuth direction. SPP gives a phase difference of an integral multiple of 2π in one round denoted by the topological charge, resulting in the conversion of a plane wave into an optical vortex with a spiral wavefront. Vortex waves have orbital angular momentum (OAM) [30,31]. Optical vortex generated using SPP has been widely reported and it has been demonstrated in inducing ablation, needle formation and controlling the chirality of nanostructures on metal and silicon [32-35]. In these phenomena, the energy of the laser induces the ablation. Laser-induced plasma acquires rotational motion due to the OAM of the optical vortex, leading to the formation of nanoneedle structures [36].

In the THz regime, the combination of THz radiation and OAM technology has recently attracted attention due to its promising applications in communication [37]. Using flexible polymeric materials with low permittivity, absorbance, and dispersion in the THz region [38,39], SPP can be used to form THz vortex effectively [40,41,42]. The observation of the topological charge of a THz vortex beam directly by using a THz camera with tilted lens focusing and radial defect introduction has been demonstrated [41].

Makoto Nakajima

nakajima.makoto.ile@osaka-u.ac.jp

1 Institute of Laser Engineering, Osaka University, Suita, Osaka 565-0871, Japan

2 Graduate School of Science and Engineering, Kansai University, Suita, Osaka, 564-8680, Japan

3 Graduate School of Engineering, Faculty of Engineering, Chiba University, Chiba, Chiba, 263-8522, Japan

4 Device Technology Research Institute, National Institute of Advanced Industrial Science & Technology (AIST), Tsukuba, Ibaraki, 305-8568 Japan

5-Institute of Scientific and Industrial Research, Osaka University, Ibaraki, Osaka, 567-0047, Japan

However, up to now, there has been no report on THz vortex beam-induced ablation and laser machining.

Laser-induced periodic surface structures (LIPSS) formation, which is another attractive phenomenon, provides a simple way of surface nanostructuring. LIPSS can be classified according to their period as Low Spatial Frequency LIPSS (LSFL) or as High Spatial Frequency LIPSS (HSFL). LSFL has a periodicity close to the laser wavelength and can be observed mostly on metals and semiconductors with orientation generally dependent on the laser beam polarization and laser processing conditions. On the other hand, HSFL is characterized by a period smaller than half of the laser wavelength. Depending on the material, the orientation of HSFL can be parallel or perpendicular to the beam polarization. Except for the wavelength, the periodicity of LIPSS can be controlled by the angle of incidence, laser power or pulse duration, whereas the direction of LIPSS can be controlled by the polarization of the laser beam. The great flexibility and variability of the produced LIPSS following the laser and processing parameters allow tailoring of surface mechanical, biological or optical properties [43].

In this paper, we demonstrate the THz vortex beam-induced ablation phenomena for the first time. The ablation marks, including LIPSS, on surfaces of phase change memory (PCM) materials were experimentally investigated in detail.

2 Experiment

2.1 Sample preparation

PCM has been widely utilized for applications in nonvolatile electrical memory as well as in rewritable optical discs [44]. The SET-RESET memory operation, also known as crystalline-amorphous phase transition, is realized by applying electrical or optical pulses that induce thermal annealing or melt-quench disordering effects on the structure of PCM [45]. Since this structural phase transition results in significant differences in electrical resistivity and optical reflectivity, data storage can be realized [46].

We prepared two types of PCM samples because of the low ablation threshold of these materials [47,48]. One of the prepared PCM was amorphous $Ge_2Sb_2Te_5$ (GST), which is a 100-nm GST thin film deposited on 500-µm-thick Al_2O_3 substrate by DC magnetron sputtering at room temperature. A stoichiometric $Ge_2Sb_2Te_5$ target was used as the sputtering source. A 20-nm SiO_2 protective layer was deposited on the sample to prevent oxidation. The as-grown film was amorphous and did not undergo any annealing. The other PCM sample was a superlattice of GeTe and Sb_2Te_3 layers (GT-ST) which has a low ablation threshold during experiment of about 0.7 J/cm^2. The multilayered structures were sputter-deposited on a high-resistivity Si substrate (> 10000 Ω·cm). The sample was composed of 20 alternately stacked layers of 0.85-nm GeTe sublayers and 1.0-nm Sb_2Te_3 sublayers. Fabrication details of the multilayered structure can be seen in a preceding paper [48].

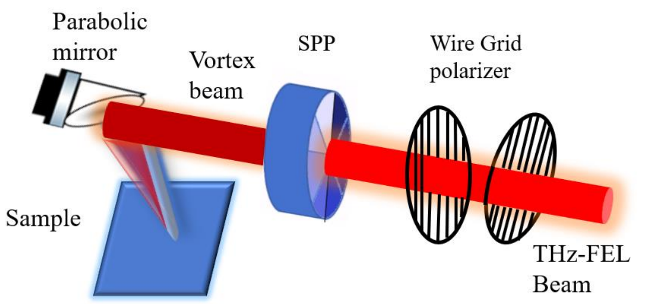

Fig. 1 Schematic diagram of the experimental configuration for sample irradiation with THz vortex beam.

2.2 THz vortex beam irradiation

Figure 1 shows a schematic illustration of the experimental setup. Intense THz pulses were generated with the 40-MeV L-band (1.3 GHz) electron linac at the Institute of Scientific and Industrial Research, Osaka University [49]. The FEL consists of a permanent magnet wiggler. By varying the wiggler gap, the wavelength of the FEL beam is tunable from approximately 40 to 110 µm with an electron energy of 15 MeV. The FEL emits intense THz macropulses which consist of a train of ~160 micropulses with approximately 6-µs duration and 37-ns interval between individual micropulses. The macropulses have a duration of up to ~6 µs, depending on the FEL operational conditions, at a repetition frequency of 5 Hz. The maximum macropulse energy was >40 mJ on average at the center wavelength of 75 µm (4 THz). We treat the macropulse as one pulse in this study. To generate a first-order THz vortex beam, the linearly polarized THz pulses emitted from the THz-FEL were directed through a continuous SPP designed for 4 THz. The SPP with dimensions of 40 mm (aperture) × 1.7mm (thickness) is made of Tsurupica (refractive index, n is ~1.52 in the 1–6 THz frequency range), and it constitutes one turn of a spiral stairway with a step height of 144 ± 3 µm (corresponding to an accuracy of 1%). Thus, it provides an azimuthal phase shift of 2π for 4-THz radiation (i.e., at a wavelength of 75 µm), resulting in a topological charge of l

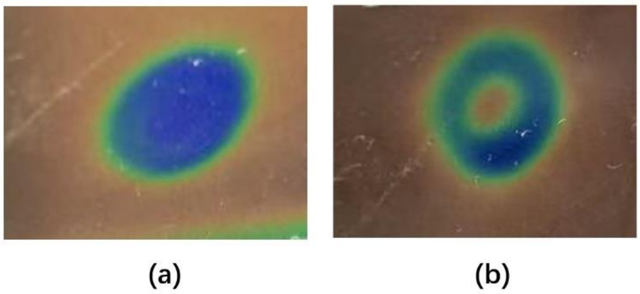

Fig. 2 Image of THz beam in the thermochromic liquid crystal as a result of 50 shots of THz-FEL pulse irradiation (a) without and (b) with SPP.

= 1. The SPP based on Tsurupica olefin polymer has a high transmission and low dispersion in the THz region. The 1.7 mm-thick Tsurupica exhibits high transmission (>86% before Fresnel correction, >92% after Fresnel correction) at a frequency range of 2–4 THz. Thus, the SPP does not have any negative impacts on the spatial form of the THz output along the azimuthal direction. Unlike a quarter-wave plate, SPP does not alter the polarization state of light. Hence, when the linearly polarized Gaussian THz beam passes through the SPP grating, the resulting THz vortex beam (in the first diffractive order) is still linearly polarized. In fact, the SPP can be applied to laser pulses with any polarization states [41,42]. We did not use a commercial electronic THz camera for the FEL pulse evaluation due to the possibility of damage induced by the high-intensity source. Instead, we used a thermochromic liquid crystal [50-52] which can change color at a specified temperature starting at red (25 ^{o}C), changing to green (27 ^{o}C) then blue (30 ^{o}C). The colors reflect the beam intensity profile of the THz beam. Figures 2 (a) and (b) show the intensity profiles of the THz beams without and with SPP, respectively, after 50 shots. The blue color corresponds to the high intensity distribution of THz pulses. We observed the singularity point at the center of the THz beam in Fig 2(b) where there is a decrease in intensity. This result indicates that the Gaussian beam of THz pulses is transformed into a vortex beam by the SPP. We thus succeeded in obtaining a THz vortex beam with high-intensity pulses from a THz FEL.

The fabricated samples were then irradiated with the generated THz vortex beam. The THz vortex beam was focused onto the samples using a 90° off-axis parabolic mirror with effective focal length f = 25.4 mm, focusing the spot size to a diameter of 0.6 mm. A pair of wire grid polarizers was used to control the intensity of the incident THz pulse. The highest energy density in the illuminated area is 2.7 J/cm^2. The number of pulses was controlled by shutting the window from the laser source. The samples were placed on a translational stage and were moved to expose a new sample area after each irradiation. The ablation marks were investigated using an optical microscope (Keyence VHX6000).

3 Results

The ablation of GT-ST sample induced by THz-FEL is discussed first. The ablation pattern on the sample surface after 10 shots of THz pulse irradiation is shown in the inset of Fig. 3. The microscope image shows an annular shape, and the singularity of the incident vortex beam is apparently observed at the center of the ablation pattern. We measured the depth profile of the ablation mark using a laser microscope (Keyence VK8700) which scans a sample surface with a laser (λ = 658 nm, maximum output = 0.9 mW) to evaluate the surface profile. The spatial and height resolutions are 1.4 μm and 10 nm, respectively. The depth profile along the diameter of the ablation mark is shown in Fig. 3. A value of 0 μm is set as the height of the unirradiated area of the sample. Based on the depth profile measurement, the sample surface has been removed by about 10 μm due to ablation. On the other hand, the central part has the same height as the unirradiated parts indicating that no ablation occurred at the center which coincides with the singularity of the incident vortex beam. The ablation mark formed a cylindrical protrusion at the center with a diameter of 30 μm. This characteristic is very similar to the results of optical vortex beam excitation [33,34,35,53]. The diameter of 30 μm is corresponding to 40 % of the wavelength (75 μm) of the incident beam.

To investigate the effect of the OAM polarity of the vortex beam, single-shot irradiation of the sample was performed

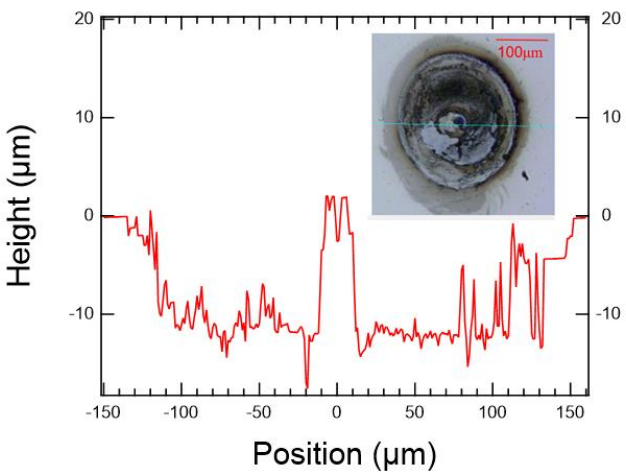

Fig. 3 Microscope image of the sample after 10 shots of irradiation with 4THz vortex beam (inset) and the corresponding depth profile along the center denoted by the horizontal aqua line.

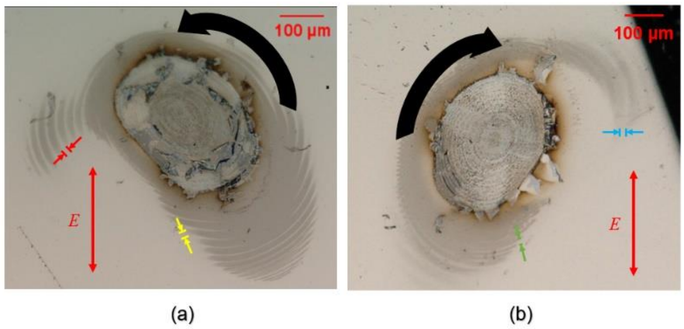

Fig. 4 (a, b) Microscope images of the sample after irradiation of 4 THz vortex beam generated using opposite directions of SPP.

with SPP in reverse directions. Figure 4 shows the microscope images of the spot irradiated with the SPP in opposite directions. The incident polarization *E* is depicted by the vertical red arrows. The two images were observed in the same irradiation condition excluding the OAM polarity which is controlled by the direction of the SPP. THz-induced undulations with a spiral pattern are observed at outside of the main ablation spot. The period of the undulations varies depending on the location within the irradiation spot. In Fig. 4 (a), the average period across the red arrow is 15 μm whereas the average period across the yellow arrow reaches 5.7 μm. On the other hand, the average period of the undulations across the blue arrow in Fig. 4b is 11 μm, whereas the average period across the green arrow reaches 5.3 μm. For comparison between Figs. 4 (a) and (b), we arbitrarily assign the longer-period undulations (15, 11 μm) as the outermost undulations. If we follow a rotation direction going from the shorter-period undulations (5.7, 5.3 μm) to the longer-period undulations as denoted by the black curved arrows, we see that the ablation marks in Figs. 4 (a) and (b) have opposite rotation directions. We can also infer that the two ablation patterns have chirality symmetry. This result shows that the OAM polarity influences the orientation of the ablation pattern. Furthermore, the spiral undulations can be attributed to the torque induced by the THz vortex beam. During the laser ablation process, the OAM of the vortex beam generates a torque, which is not

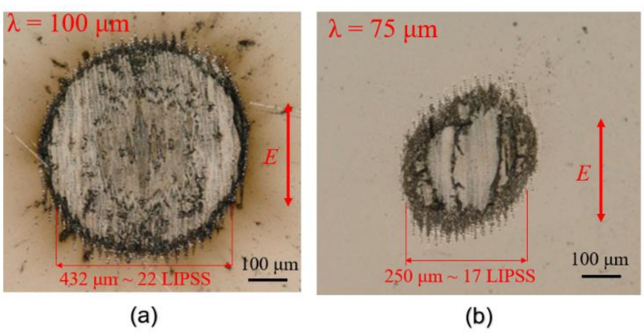

Fig. 5 Microscope images of the sample after 30-mJ irradiation with (a) 3 THz without wire grid polarizers and (b) 4 THz.

strong enough to cause damage to the surface of the irradiated object, but which rotates the plasma generated by the laser and the blown particles from laser irradiation.

The results of GST ablation are discussed next. To investigate the effect of the THz-FEL wavelength, we performed irradiation with 5 shots of 3 THz (λ = 100 μm) and 4 THz (λ = 75 μm) pulses by changing the wiggler gap of the THz-FEL. Figures 5 (a) and (b) show the microscope images of the samples irradiated with 3 THz and 4 THz, respectively, without the use of SPP. The incident polarization *E* is depicted by the vertical red arrows. Since the incident beam is not a vortex beam, the ablation pattern is not annular in shape. The LIPSS periodic intervals are 14.7 μm and 19.6 μm for Figs. 5 (a) and (b), respectively. In both conditions, the period of the LIPSS is 1/5 of the incident wavelength. The induced LIPSS is categorized to HSFL. The formation of LIPSS has been reported in various kinds of materials irradiated by visible and near-infrared optical pulses with fluence slightly below the ablation threshold [54]. The values of the LIPSS periodicity strongly depend on the sample materials and the experimental conditions [55-57].

For comparison, we also investigated the LIPSS generation with the use of SPP. Figures 6 (a) and (d) show the microscope images of the ablation pattern with LIPSS induced by a THz vortex beam generated using opposite SPP orientations, thus opposite polarity of OAM. Annular ablation marks induced by the THz vortex beam are clearly observed. The absence of ablation mark at the center is due to the singularity of the incident THz vortex beam. Vertical LIPSS patterns are also observed in Figs. 6 (a) and (d). This vertical direction is almost parallel to the polarization of the incident THz beam. Figs. 6 (b) and (c) are enlargements of the upper and lower parts of Fig. 6 (a), respectively, whereas Figs. 6 (e) and (f) are also the enlargements of Fig. 6 (d). The orientations of the upper and lower parts of the LIPSS have different deflections from the vertical. To clearly show this, we vertically aligned the upper parts of the LIPSS and compared the deflections of the lower parts. We observed a counterclockwise deflection (8°) in Fig. 6(c) and a clockwise deflection (-8°) in Fig. 6(f) with respect to the vertical, showing opposite directions of deflections with opposite SPP orientations. The difference in the direction of the deflection can be explained by the difference in the polarity of OAM of the incident THz vortex beam.

Taking a closer look at the magnified images in Figs. 6 (b), (c), (e), and (f), finer horizontal LIPSS can be seen which are similar to the reported shapes of Si and SiO_2 [20,58]. It can also be seen in Fig. 5, so it is not induced by

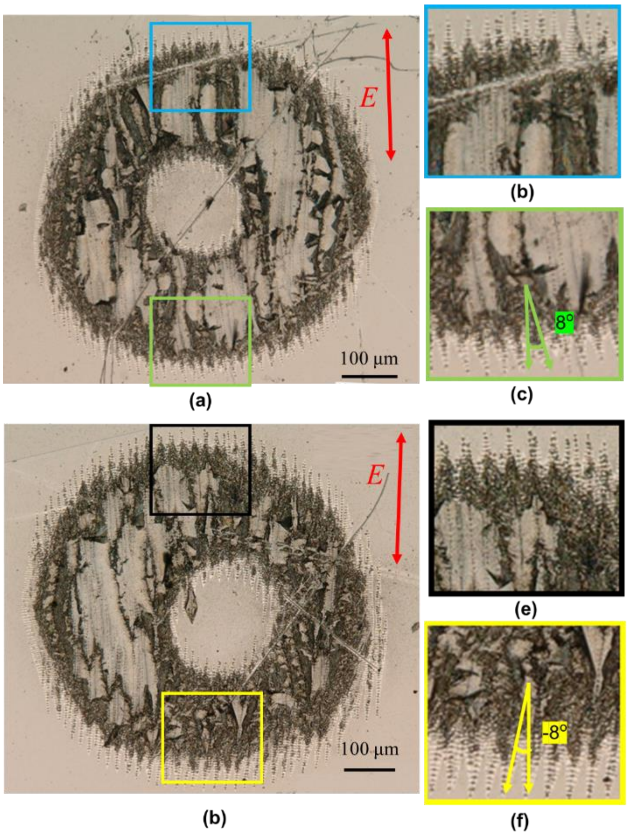

Fig. 6 (a, d) Microscope images of the sample after 10 shots of irradiation with 4 THz vortex beam with a topological charge of $l = \pm 1$ generated by reversing the SPP direction; (b, c) upper part of the ablation mark and deflection in the lower part of the ablation mark in (a); (b, c) upper part of the ablation mark and deflection in the lower part of the ablation mark in (d). The deflection is

the SPP element. This LIPSS formation perpendicular to the polarization direction can be associated with the SiO_2 protective layer of our sample. Due to the weaker beam intensity distribution at the edge of the ablation area, LIPSS formation in SiO_2 was observed. It is known that for LIPSS in SiO_2 with 20 nm thickness, the orientation is perpendicular to the polarization direction [58].

In contrast to previous studies utilizing optical vortex, we did not observe chiral needle-like structures after irradiation with an intense THz vortex. This can be explained by the difference in the torque induced by optical and THz vortex beams. The rotational motion of the plasma still conforms to the theorems of classical mechanics. Although it will be affected by the electromagnetic force and its own viscosity, the torque that makes it rotate is the most important factor. The torque can be estimated from the absorbed energy of the vortex beam by the sample target using classical electromagnetic theory [32,33,34,35,59]. When simply considering the paraxial limit, the torque T exerted by a linearly polarized vortex beam incident on a sample is given by $T = \frac{P}{\omega} l$, where P, ω, and l are the absorbed power in the sample, the frequency of the incident beam, and the OAM state, respectively. The torque generates a rotational acceleration a expressed as $a = T/I = \frac{2P}{\omega \pi \sigma r^4} l$ (I: inertia moment, σ: illuminated area density, r: radius of radiation spot). Here we considered the approximation that the formed plasma distribution is uniform on the target. This equation shows that the rotation acceleration is proportional to $\omega^{-1} r^{-4}$. Considering the long wavelengths of THz waves, the beam size is bigger thus resulting in a much smaller rotational acceleration due to the term r^{-4}. For comparison between THz ($\omega = 16$ meV, $r = 300$ µm) and optical ($\omega = 1.5$ eV, $r = 10$ µm) excitation cases, the estimated rotation acceleration induced by THz pulses is about 1/8600 smaller than that of the optical case [33]. Our observations in Figs. 4 and 6 are not dominant compared to that of optical vortex experiments, but the effects are experimentally confirmed by using intense THz free electron pulses.

4 Conclusion

We investigated the ablation induced by intense THz vortex beams. Aside from LIPSS formation, annular ablation pattern due to the singularity of the vortex beam was demonstrated. Moreover, by using an intense THz source, we have shown that the polarity of the OAM carried by the THz vortex beam influences the orientation of the ablation pattern. These results show the first demonstration of the application of THz vortex beam in ablation.

Acknowledgements This work was supported by the Japan Society for the Promotion of Science (JSPS) through the Grants-in-Aid for Scientific Research (KAKENHI) Grant No.JP20H02206, JP22H01980, JP19K02599 and JST CREST Grant No. JPMJCR1903. We thank to Prof. M. Nagai of Osaka University for the optical microscopy measurements.

Declarations

Conflict of Interest The authors declare no conflict of interest.

Reference

1. M. Hangyo, Jpn. J. Appl. Phys. 54, 120101 (2015). https://doi.org/10.7567/JJAP.54.120101

2. H. Y. Hwang, S. Fleischer, N, C. Brandt, B. G. Perkins Jr, M.Liu, K. Fan, A. Sternbach, X. Zhang, R.D. Averitt, K. A. Nelson, J. Mod. Opt. 62, 1447-1479 (2015). https://doi.org/10.1080/09500340.2014.918200
3. T. Kampfrath, K. Tanaka, and K. A. Nelson, Nat. Photonics 7, 680-690 (2013). https://doi.org/10.1038/nphoton.2013.184
4. M. Liu, H. Y. Hwang, H.Tao, A. C. Strikwerda, K. Fan, G. R. Keiser, A. J. Sternbach, K. G. West, S. Kittiwatanakul, J. Lu, S. A. Wolf, F. G. Omenetto, X. Zhang, K. A. Nelson, R. D. Averitt, Nature 487, 345-348 (2012). https://doi.org/10.1038/nature11231
5. H. A. Hafez, X. Chai, A. Ibrahim, S. Mondal, D. Férachou, X. Ropagnol, T. Ozaki, J. Opt. 18, 093004 (2016). https://doi.org/10.1088/2040-8978/18/9/093004
6. T. Kurihara, K. Hirota, H. Qiu, K. T. N. Phan, K. Kato, G. Isoyama, M, Nakajima, Sci. Rep. 10, 7321 (2020). https://doi.org/10.1038/s41598-020-64147-5
7. K. Kato, H. Qiu, E. M. Khutoryan, Y. Tatematsu, M. Tani, T. Idehara, Y. Yamaguchi, M. Fukunari, Y. Maeda, K. Takayama, Y. Minami, M. J. F. Empizo, T. Kurihara, K. Yamanoi, T. Shimizu, K. Takano, N. Sarukura, T. Fukuda, M. Yoshimura, M. Nakajima, Appl. Phys. Lett. 111, 031108 (2017). https://doi.org/10.1063/1.4994316
8. D. Li, M. Nakajima, M. Tani, J. Yang, H. Kitahara, M. Hashida, M. Asakawa, W. Liu, Y. Wei, Z, Yang, Sci. Rep. 9, 6804 (2019). https://doi.org/10.1038/s41598-019-43072-2
9. S. Ohkoshi, M. Yoshikiyo, K. Imoto, K. Nakagawa, A. Namai, H. Tokoro, Y. Yahagi, K. Takeuchi, F. Jia, S. Miyashita, M. Nakajima, H. Qiu, K. Kato, T. Yamaoka, M. Shirata, K. Naoi, K. Yagishita, H. Doshita, Adv. Mater. 32, 2004897 (2020). https://doi.org/10.1002/adma.202004897
10. T. Kurihara, H. Watanabe, M. Nakajima, S. Karube, K. Oto, Y.C. Otani, T. Suemoto, Phys. Rev. Lett. 120, 107202 (2018). https://doi.org/10.1103/PhysRevLett.120.107202
11. G. Fitzky, M. Nakajima, Y. Koike, A. Leitenstorfer, T. Kurihara, Phys. Rev. Lett. 127, 107401 (2021), https://doi.org/10.1103/PhysRevLett.127.107401
12. M. Nakajima, A. Namai, S. Ohkoshi, T. Suemoto, Opt. Express, 18 (2010). https://doi.org/10.1364/OE.18.018260
13. K. Yamaguchi, M. Nakajima, T. Suemoto, Phys. Rev. Lett. 105, 237201 (2010) https://doi.org/10.1103/PhysRevLett.105.237201
14. K. Yamaguchi, T. Kurihara, H. Watanabe, M. Nakajima, T. Suemoto, Phys. Rev. B 92, 064404 (2015). https://doi.org/10.1103/PhysRevB.92.064404
15. H. Qiu, T. Kurihara, H. Harada, K. Kato, K. Takano, T. Suemoto, M. Tani, N. Sarukura, M. Yoshimura, M. Nakajima, Opt. Lett. 43, 1658-1661 (2018). https://doi.org/10.1364/OL.43.001658
16. M. Nakajima, N. Takubo, Z. Hiroi, Y. Ueda, T. Suemoto, Appl. Phys. Lett. 92, 011907 (2008). https://doi.org/10.1063/1.2830664
17. V. C. Agulto, K. Toya, T. N. K. Phan, V. K. Mag-usara, J. Li, M. J. F. Empizo, T. Iwamoto, K. Goto, H. Murakami, Y. Kumagai, N. Sarukura, M. Yoshimura, M. Nakajima, Appl. Phys. Lett. 118, 042101 (2021). https://doi.org/10.1063/5.0031531
18. V. C. Agulto, T. Iwamoto, H. Kitahara, K. Toya, V. K. Mag-usara, Ma.i Imanishi, Yusuke Mori, Masashi Yoshimura & Makoto Nakajima Sci. Rep. 11, 18129 (2021). https://doi.org/10.1038/s41598-021-97253-z
19. K. Makino, S. Kuromiya, K. Takano, K. Kato, M. Nakajima, Y. Saito, J. Tominaga, H. Iida, M. Kinoshita, T. Nakano, ACS Appl. Mater. Interfaces, 8, 32408-32413 (2016). https://doi.org/10.1021/acsami.6b11418
20. K. Makino, K. Kato, K. Takano, Y. Saito, J. Tominaga, T. Nakano, G. Isoyama, M. Nakajima, Sci. Rep., vol. 8, 2914 (2018). https://doi.org/10.1038/s41598-018-21275-3
21. L. Allen, M. W. Beijersbergen, R. J. C. Spreeuw, J. P. Woerdman, Phys. Rev. A 45, 8185–8189 (1992). https://doi.org/10.1103/PhysRevA.45.8185
22. M. Padgett, R. Bowman, Nat. Photon 5, 343-348 (2011). https://doi.org/10.1038/nphoton.2011.81
23. C. Paterson, Phys. Rev. Lett. 94, 153901 (2005). https://doi.org/10.1103/PhysRevLett.94.153901
24. L. Li, F. Li, Phys Rev. E 88, 033205 (2013). https://doi.org/10.1103/PhysRevE.88.033205
25. C. Hnatovsky, V. G. Shvedov, W. Krolikowski, A. V. Rode, Opt. Lett. 35, 3417-3419 (2010). https://doi.org/10.1364/OL.35.003417
26. G. A. Swartzlander, E. L. Ford, R. S. Abdul-Malik, L. M. Close, M. A. Peters, D. M. Palacios, D. W. Wilson, Opt. Express 16, 10200-10207 (2008). https://doi.org/10.1364/OE.16.010200
27. A. Niv, Y. Gordodetski, V. Kleiner, E. Hasman, Opt. Lett 33, 2910-2912 (2008). https://doi.org/10.1364/OL.33.002910
28. C. Min, J. Liu, T. Lei, G. Si, Z. Xie, J. Lin, L. Du, X. Yuan, Laser Photonics Rev. 10, 978-985 (2016). https://doi.org/10.1002/lpor.201600101
29. R. C. Devlin, A. Ambrosio, D. Wintz, S. L. Oscurato, A. Y. Zhu, M. Khorasaninejad, J. Oh, P. Maddalena, F. Capasso, Opt. Express 25, 377-393 (2017). https://doi.org/10.1364/OE.25.000377
30. V. V. Kotlyar, A. A. Almazov, S. N. Khonina, V. A. Soifer, H. Elfstrom, J. Turunen, J. Opt. Soc. Am. A 22, 849-861 (2005). https://doi.org/10.1364/JOSAA.22.000849
31. Y. Sasaki, K. Yamaguchi, J. Shibakawa, K. Miyamoto, T. Omatsu, Appl. Opt. 56, 8075-8080 (2017). https://doi.org/10.1364/AO.56.008075
32. J. Hamazaki, R. Morita, K. Chujo, Y. Kobayashi, S. Tanda, T. Omatsu, Opt. Express 18, 2144-2151 (2010). https://doi.org/10.1364/OE.18.002144
33. K. Toyoda, K. Miyamoto, N. Aoki, R. Morita, T. Omatsu, Nano

Lett. 12, 3645–3649 (2012). https://doi.org/10.1021/nl301347j
34. K. Toyoda, F. Takahashi, S. Takizawa, Y. Tokizane, K. Miyamoto, R. Morita, T. Omatsu, Phys. Rev. Lett. 110, 143603, (2013). https://doi.org/10.1103/PhysRevLett.110.143603
35. F. Takahashi, K. Miyamoto, H. Hidai, K. Yamane, R. Morita, T. Omatsu, Sci. Rep. 6, 21738 (2016). https://doi.org/10.1038/srep21738
36. S. Paul, S. I. Kudryashov, K. Lyon, and S. D. Allen, "Nanosecond-laser plasma-assisted ultradeep microdrilling of optically opaque and transparent solids," J. Appl. Phys. 101, 043106 (2007). https://doi.org/10.1063/1.2434829
37. H. Yang, S. Zheng, W. He, X. Yu and X. Zhang, Chi Commu., 18, 131-152 (2021). https://doi.org/10.23919/JCC.2021.05.009.
38. A. Podzorov, G. Gallot, Appl. Opt. 47, 3254-3257 (2008). https://doi.org/10.1364/AO.47.003254
39. S. Walia, C. M. Shah, P. Gutruf, H. Nili, D. R. Chowdhury, W. Withayachumnankul, M. Bhaskaran, S. Sriram, Appl. Phys. Rev. 2, 011303 (2015) https://doi.org/10.1063/1.4913751
40. K. Miyamoto, K. Sano, T. Miyakawa, H. Niinomi, K. Toyoda, A. Vallés, T. Omatsu, Opt. Express 27, 31840-31849 (2019). https://doi.org/10.1364/OE.27.031840
41. K. Miyamoto K. Suizu T. Akiba, T. Omatsu, Appl. Phys. Lett. 104, 261104 (2014). https://doi.org/10.1063/1.4886407
42. K. Miyamoto, B. J. Kang, W. T. Kim, Y. Sasaki, H.Niinomi, K. Suizu, F. Rotermund, T. Omatsu, Sci Rep 6, 38880 (2016). https://doi.org/10.1038/srep38880
43. J. Bonse and J. Krüger, "Femtosecond laser-induced periodic surface structures" J. Laser Appl. 24, 042006 (2012). https://doi.org/10.2351/1.4712658
44. S. Raoux, R. M. Shelby, J. Jordan-Sweet, B. Munoz, M. Salinga, Y. C. Chen, Y. H. Shih, E. K. Lai, M. H. Lee, Microelectron. Eng. 85, 2330-2333 (2008). https://doi.org/10.1016/j.mee.2008.08.004
45. J. Momand, R. Wang, J. E. Boschker, M. A. Verheijen, R. Calarco, and B. J. Kooi, Nanoscale 7, 19136 (2015). https://doi.org/10.1039/C5NR04530D
46. N. Yamada, E. Ohno, K. Nishiuchi, N. Akahira, J. Appl. Phys. 69, 2849 (1991). https://doi.org/10.1063/1.348620
47. K. Makino, K. Kato, Y. Saito, P. Fons, A. V. Kolobov, J. Tominaga, T. Nakano, M. Nakajima. Opt. Lett. 44, 1355-1358 (2019). https://doi.org/10.1364/OL.44.001355
48. K. Makino, K. Kato, Y. Saito, P. Fons, A. V. Kolobov, J. Tominaga, T. Nakano, M. Nakajima, J. Mater. Chem. C 7, 8209-8215 (2019). https://doi.org/10.1364/OL.44.001355
49. K. Kawase, M. Nagai, K. Furukawa, M. Fujimoto, R. Kato, Y. Honda, G. Isoyama, Nucl. Instrum. Methods Phys. Res. A 960, 163582 (2020). https://doi.org/10.1016/j.nima.2020.163582
50. Y. Tadokoro, T. Nishikawa, B. Kang, K. Takano, M. Hangyo, M. Nakajima, Opt. Lett. 40, 4456-4459 (2015). https://doi.org/10.1364/OL.40.004456
51. L. Wang, R. Xiao, S. Yang, H. Qiu, Z. Shen, P. Lv, C. Zhang, W. Hu, M. Nakajima, B.Jin, Y. Lu, Opt. Lett. 45, 5892-5895 (2020). https://doi.org/10.1364/OL.405695
52. L. Wang, H. Qiu, T.N.K. Phan, K. Kato, B. Kang, K. Takano, Y. Lu, L. Chen, P. Lv, K. Yu, W. Wei, B. Jin, M. Nakajima, Appl. Sci. 8, (2018). https://doi.org/10.3390/app8122580
53. C. Hnatovsky, V. G. Shvedov, N. Shostka, A. V. Rode, W. Krolikowski, Opt. Lett. 37, 226-228 (2012). https://doi.org/10.1364/OL.37.000226
54. T.T.D. Huynh, N. Semmar, Appl. Phys. A 116, 1429–1435 (2014). https://doi.org/10.1007/s00339-014-8255-0
55. A. Irizawa, S. Suga, T. Nagashima, A. Higashiya, M. Hashida, S. Sakabe, Appl. Phys. Lett. 111, 251602 (2017). https://doi.org/10.1063/1.5006014
56. P. Hauschwitz, J. Martan, R. Bičišťová, C. Beltrami, D. Moskal, A. Brodsky, N. Kaplan, J. Mužík, D. Štepánková, J. Brajer, D. Rostohar, J. Kopeček, L. Prokešová, M. Honner, V. Lang, M. Smrž T. Mocek. Sci Rep 11, 22944 (2021). https://doi.org/10.1038/s41598-021-02290-3
57. H. Hikage, N. Nosaka S. Matsuo Appl. Phys. Express 10 112701 (2017).
58. P. Nürnberger, H. M. Reinhardt, H. Kim, E.Pfeifer, M. Kroll, S. Müller, F. Yang, N. A. Hampp, Appl. Surf. Sci. 425 (2017) 682-688, https://doi.org/10.1016/j.apsusc.2017.06.316
59. M. E. J. Friese, J. Enger, H. Rubinsztein-Dunlop, N. R. Heckenberg, Phys. Rev. A 54, 1593 (1996). https://doi.org/10.1103/PhysRevA.54.1593